ADVANCED MATERIALS INTERFACES

www.advmatinterfaces.de

Check for updates

A Novel Nanocomposite with Superior Antibacterial Activity: A Silver-Based Metal Organic Framework Embellished with Graphene Oxide

Mostafa Dadashi Firouzjaei, Ahmad Arabi Shamsabadi, Mohammad Sharifian Gh., Ahmad Rahimpour, and Masoud Soroush**

Silver-based nanomaterials have attracted considerable attention due to their antimicrobial activities. In this work, a silver (Ag)-based metal organic framework (Ag-MOF) is embellished with graphene-oxide (GO), leading to the fabrication of a novel Ag-based nanocomposite (GO-Ag-MOF) whose biocidal activity is higher than those of Ag-MOF and GO nanomaterials. The nanocomposite is characterized using X-ray photoelectron spectroscopy, transmission electron microscopy, scanning electron microscope, Fourier transform infrared spectra, ultraviolet–visible absorption spectra, X-ray powder diffraction, dynamic light scattering, and nitrogen gas adsorption/desorption. The characterization shows that the Ag-MOF nanoparticles are uniformly dispersed on the GO nanosheets surfaces without any agglomeration. Toxicities of GO-Ag-MOF, Ag-MOF, and GO are assessed against the Gram-negative bacteria, *Escherichia coli* and the Gram-positive bacteria, *Bacillus subtilis* using the growth curve, fluorescence imaging, and flow cytometry methods. GO-Ag-MOF shows an outstanding antibacterial activity (higher than those of the Ag-MOF and GO alone). The interaction of GO-Ag-MOF and Ag-MOF with the bacteria leads to the extirpation of 95 and 85% of live bacteria cells, respectively. This study indicates that GO-Ag-MOF is a promising antibacterial nanocomposite, especially for biomedical applications.

1. Introduction

The existence and propagation of harmful microorganisms have caused human and animal health and process-industry problems – such as the corrosion of the metallic surfaces in fluid systems[1] and biofouling in membrane processes.[2] The toxicity and irritancy of existing antibacterial agents, the creation of undesirable by-products in biocidal processes, and increasingly higher resistance of bacteria to the agents, have motivated many studies to replace these agents with nanomaterials having superior disinfection properties.[3] Biocidal nanoparticles have potential to address these problems.

Carbon-based nanomaterials have numerous applications and have impacted many technologies.[4] For example, the environmental technology has greatly benefited from the ability of scientists to recognize, discriminate, and synthesize various types of carbon-based nanomaterials like graphene-oxide (GO).[5,6] GO is an important carbon-based material, which is synthesized using different methods such as Staudenmeier and Hummers's and Brodie's.[7] The thickness of a GO nanosheet strongly affects the GO properties and applications.[8,9] The thickness of a GO nanosheet is typically around 1 nm.[8] In addition to the size and thickness of GO, its various oxygen functional groups endow it with excellent surface properties.[9] Its functional groups include its carboxyl groups on the edges and epoxide and hydroxyl groups on the basal planes.[10] These functional groups provide sites for chemical reactions and GO modifications. Besides all these properties, GO has good antibacterial properties that are of great interest in biomedical applications.[11] The antibacterial properties of GO are originated from physical and chemical interactions between GO and bacteria cell membranes.

Several mechanisms have been proposed for the antibacterial activity of GO. Akhavan et al.[12,13] reported that sharp edges of GO nanowalls damage bacteria cell membranes. Hu et al.[14] found that the oxidative stress of the GO damages *Escherichia* (*E.*) *coli* cells. Similarly, Kotchey et al.[15] proposed that the cellular membrane of the bacteria is damaged due to superoxide

M. Dadashi Firouzjaei
Department of Materials Science and Engineering
Sharif University of Technology
Tehran 11155-8639, Iran

A. Arabi Shamsabadi, Prof. M. Soroush
Department of Chemical and Biological Engineering
Drexel University
Philadelphia, PA 19104, USA
E-mail: soroushm@drexel.edu

M. Sharifian Gh.
Department of Chemistry
Temple University
Philadelphia, PA 19122, USA

Prof. A. Rahimpour
Department of Chemical Engineering
Babol Noushirvani University of Technology
Shariati Ave., Babol 47148-71167, Iran
E-mail: ahmadrahimpour@yahoo.com, ahmadrahimpour@nit.ac.ir

The ORCID identification number(s) for the author(s) of this article can be found under https://doi.org/10.1002/admi.201701365.

DOI: 10.1002/admi.201701365

 © 2018 WILEY-VCH Verlag GmbH & Co. KGaA, Weinheim

21967350, 2018, 11, Downloaded from https://onlinelibrary.wiley.com/doi/10.1002/admi.201701365 by Mostafa Dadashi Firouzjaei - University Of Alabama-Tuscaloosa , Wiley Online Library on [15/11/2024]. See the Terms and Conditions (https://onlinelibrary.wiley.com/terms-and-conditions) on Wiley Online Library for rules of use; OA articles are governed by the applicable Creative Commons License

anions generated by GO. Perreault et al.[16] studied the relationship between the antibacterial activity and size of GO nanoparticles. They reported that the antibacterial activity of GO nanosheets due to the oxidative mechanism, inversely depends on the size. The GO biocidal activity can be reinforced via combination with other biocidal agents.[17] Previous studies[18] have shown that silver-based nanomaterials are powerful and cost-effective antibacterial agents. Huang et al.[19] encapsulated curcumin with a polymeric micelle decorated with silver nanoparticles[20] and observed higher antibacterial activity compared to silver nanoparticles and curcumin alone. A stable nanocomposite with Ag nanoparticles, GO, and polyethylene glycol (PEG) was synthesized by Zhao et al.[21] The Ag-PEG-GO nanocomposite showed higher antimicrobial activity against *E. coli* and *Staphylococcus* (*S.*) *aureus* compared to Ag-GO. Ran et al.[22] designed a GO– (hyaluronic acid) HA–AgNPs system and reported excellent antibacterial activity against *S. aureus* and low toxicity to mammal cells.

Metal organic frameworks (MOFs) are compounds, which consist of metal ions and organic ligands.[23] Notable features of these materials are their porosity and structure.[24] As there are many metals and ligands, MOFs have a wide range of properties and applications.[25,26] For example, they have be used in drug delivery,[27] semiconductors,[28] carbon capture,[29] and gas separation.[30] The choice of the metal and organic linker directly affects MOF properties and applications.[31,32] However, the position of the linkers completely depends on the metal coordination preferences. Benzene-1,3,5-tricarboxylic acid (BTC)[33,34] and 1H-1,2,4-triazole[35,36] are common ligands, and zinc, copper, and manganese are widely used metals for MOF synthesis.[37,38] MOFs are synthesized via hydrothermal, solvothermal, solvent-free, and chemical vapor deposition.[39–45] Their antibacterial properties have received more attention in recent years.[46–48] The presence of metal ions in the MOF structure endows MOFs with bactericidal properties.[49,50] Their 3D structures stabilize the release of metal ions. Furthermore, metal ions in the MOFs structure are immune from oxidation or impurities. Organic parts of the MOFs are responsible for bonding to other materials and MOF biocompatibility.

So far, nanocomposites with antibacterial activity have been synthesized using silver nanoparticles, GO, and other materials. To the best of our knowledge, there has been no reported study of antibacterial properties of silver-based MOFs embellished with GO. This paper reports the first study of this kind. The decoration of the Ag-based MOF with GO (GO-Ag-MOF) was verified using several characterization techniques. The toxicities of the Ag-MOF and GO-Ag-MOF nanomaterials were assessed against the Gram-negative bacteria, *E. coli* and the Gram-positive bacteria, *Bacillus (B.) subtilis* using growth curve, fluorescence imaging, and flow cytometry methods.

2. Results and Discussion

2.1. Characterization of the Synthesized Nanoparticles

X-ray photoelectron spectroscopy (XPS) spectra of GO, Ag-MOF, and N1 are presented in **Figure 1**a. In addition to C (1s) and O (1s) elements which existed in all nanoparticles, Ag-MOF and N1 have also Ag (3d) in their structures. Atomic concentrations of the nanoparticles were determined from the high resolution spectra listed in **Table 1**. As can be seen, a high silver concentration was observed in the structure of Ag-MOF. However, a higher concentration of carbon in N1 than in the Ag-MOF corroborates the Ag-MOF and the GO linkage in the N1 texture. Four kinds of C atoms related to various functional groups were observed in the C1s spectrum of the GO (Figure 1b). The peak related to the nonoxygenated carbons (C—C, C=C) appeared at ≈284.7 eV.[51] Two intermediate peaks at ≈285.5 and ≈286.8 eV are assigned to C—O groups (C—OH and C—O—C).[52] Furthermore, the peak at ≈288.3 eV verifies the existence of carboxylate carbon.[53] The C/O ratio of 2.55 was obtained from the XPS data for GO nanosheets, which is in the range of 2–4 reported in the literature for the GO nanosheets synthesized with different methods.[54] The C1s spectra of the Ag-MOF and N1 (Figure 1c,d) indicates three peaks for C—C, C=C at 284.7 eV, C—O at 285.2 eV, and C=O at 288.7 eV. Furthermore, the extra peak at 286.9 eV in N1 spectrum is related to the epoxy groups of the GO in N1 structure, which verifies the presence of the GO in the N1 texture. Figure 1e,f shows the Ag 3d spectra of the Ag-MOF and N1, respectively. Two peaks ($3d_{5/2}$ and $3d_{3/2}$) appeared at around 368.2 and 374.3 eV are correspondent to Ag-O and Ag-O-Ag groups in the Ag-MOF and N1 configurations.[55] In addition to elemental analysis, the higher intensity of those peaks in the Ag-MOF spectrum also confirms the higher silver concentration in the Ag-MOF than in N1.

Figure 2 shows FT-IR spectra of the GO, Ag-MOF, and N1 nanoparticles. For the GO nanosheets all the peaks are in agreement with the literature data. The peaks can be summarized as follows: 3400 cm^{-1} (—OH stretching vibration), 1713 cm^{-1} (carbonyl C=O), 1614 cm^{-1} (hydroxyl group of carbonyl), 1164 cm^{-1} (hydroxyl group of tertiary C—OH), 1037 cm^{-1} (C—O epoxy). MOF and N1 nanoparticles have almost similar peaks related to the different bonds. However, the broader peak of Ag-MOF -GO compared to that of Ag-MOF at 2700–3500 cm^{-1} corresponds to the GO in the structure of Ag-MOF-GO. The peaks corresponding to the C—H bond are at 703–899 cm^{-1}. The two peaks at 1162 and 1193 cm^{-1} match the C—O group. The peaks appeared in the 1394–1446 cm^{-1} range are related to the C=C stretching vibration. The appearance of three peaks at 1681, 1664, and 1605 cm^{-1} reveals the reaction between carbonyl groups in BTC and silver ions.[56] The extensive area at 2700–3500 cm^{-1} is ascribed to hydroxyl group and possible adsorbed water.

Transmission electron microscopy (TEM) images of the Ag-MOF, N1, and GO are presented in **Figure 3**. The TEM images of N1 indicate a proper combination of the Ag-MOF and GO. The Ag-MOF nanoparticles distributed uniformly in the GO structure, as shown in Figure 3d. Also with respect to Figure 3a, both Ag-MOF and GO nanomaterials maintained their structural shape in N1, which is in agreement with bonds inferred from the XPS spectroscopy.

Average sizes of N1, the Ag-MOF, and GO (**Table 2**) are 160, 78, and 33 nm, respectively, which are in agreement with the TEM images. As can be seen, the proper dispersion and no agglomeration of the Ag-MOF nanoparticles in GO are in agreement with the N1 average size. The small difference between the N1 size and the sum of Ag-MOF and GO sizes indicates that the level of agglomeration was trivial.

 © 2018 WILEY-VCH Verlag GmbH & Co. KGaA, Weinheim

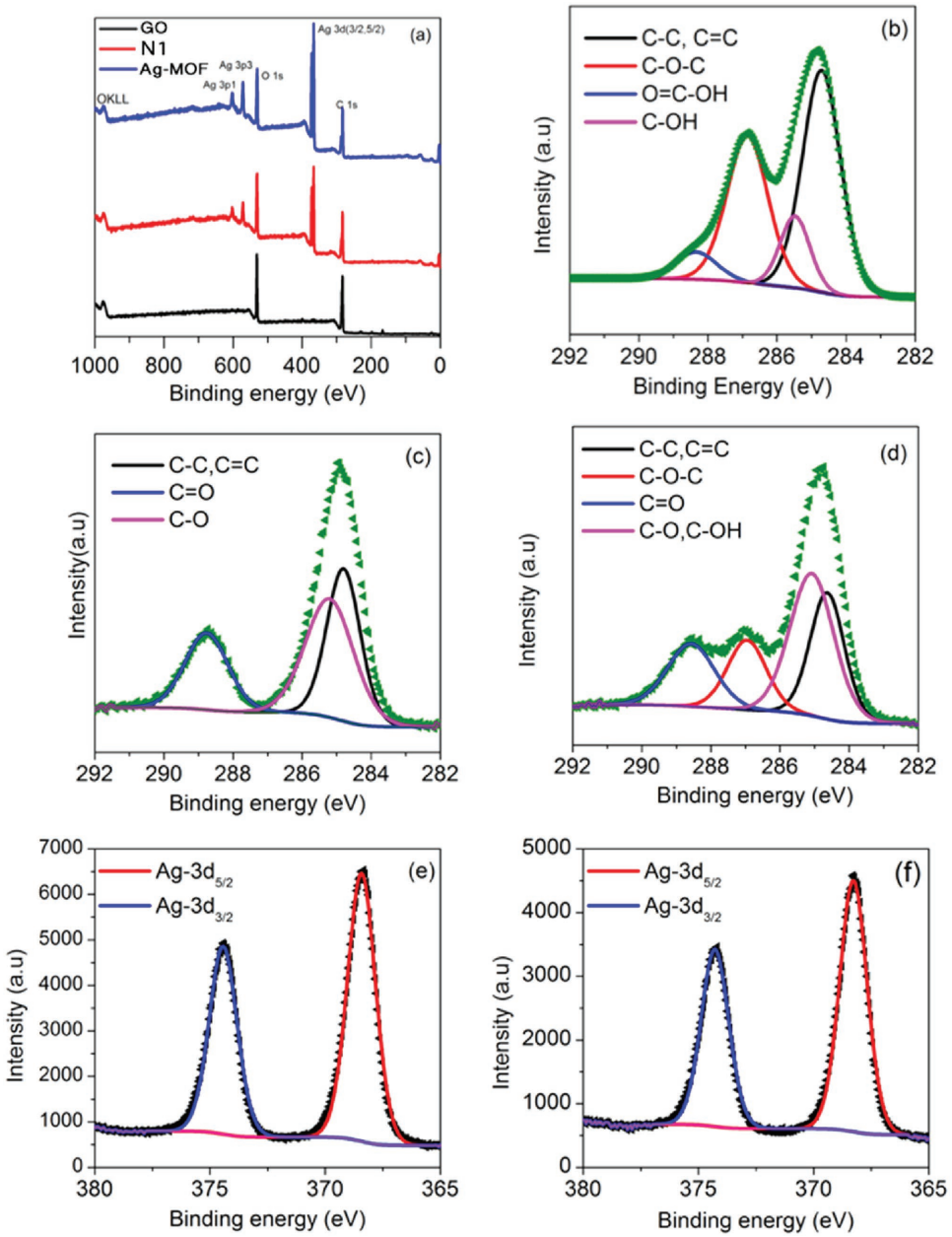

Figure 1. a) XPS spectra of Ag-MOF, GO, and N1; b) C1s spectrum of GO; c) C1s spectrum of Ag-MOF; d) C1s spectrum of N1; e) Ag 3d spectrum of Ag-MOF; and f) Ag 3d spectrum of N1.

To determine the level of the Ag-MOF interaction with GO, UV–Vis spectroscopy was performed separately for the Ag-MOF, N1, and GO (**Figure 4**c). In the UV–Vis spectrum of GO, the sharp peak at 212 nm corresponds to the electronic π–π* transition aromatic C—C bonds and the shoulder around 300 nm to the π–π* transitions of C=O bonds.[57,58] With respect to the Ag-MOF nanoparticles which have a peak at 207 nm, the UV–Vis spectrum of the N1 nanocomposite also shows a sharp peak at 209 nm that points to the interaction between the Ag-MOF and GO nanomaterials. To confirm the formation of Ag-MOF nanoparticles on GO, X-ray diffraction (XRD) characterization was performed. In XRD pattern of N1 (Figure 4b), the sharp peak at about $2\theta = 9.74°$ represents the (0 0 2) crystalline plane of GO with a *d*-spacing of 0.908 nm,[59] and at the peaks at about $2\theta = 39.2$, 43.88, 65.35, and 74.95° are attributed to the (1 1 1), (2 0 0), (2 2 0), and (3 1 1) face centered cubic crystalline

Table 1. Atomic concentrations of elements, characterized by high resolution XPS spectra.

Nanoparticles	Atomic concentration [%]		
	C [1s]	O [1s]	Ag [3d]
GO	71.84	28.16	0
Ag-MOF	58.83	31.23	8.95
N1	63.51	31.06	5.43

© 2018 WILEY-VCH Verlag GmbH & Co. KGaA, Weinheim

21967350, 2018, 11, Downloaded from https://onlinelibrary.wiley.com/doi/10.1002/admi.201701365 by Mostafa Dadashi Firouzjaei - University Of Alabama-Tuscaloosa , Wiley Online Library on [15/11/2024]. See the Terms and Conditions (https://onlinelibrary.wiley.com/terms-and-conditions) on Wiley Online Library for rules of use; OA articles are governed by the applicable Creative Commons License

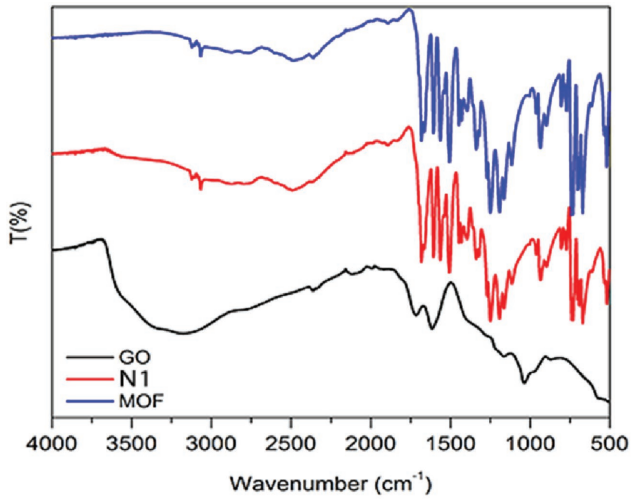

Figure 2. FT-IR spectra of GO, the MOF, and N1 nanoparticles.

planes of AgNPs,[60] which confirms the formation of silver-based Ag-MOF nanoparticles on the graphene oxide's surface.

The surface morphology of the nanocomposites can be seen in Figure 4a. The scanning electron microscopy (SEM) images of N1 show that GO and the Ag-MOF nanoparticles were combined properly. Furthermore, as explained in TEM, both GO and the Ag-MOF maintained their structures in the N1 construction.

To determine the surface area and porosity of the synthesized nanocomposites, nitrogen adsorption/desorption, and Brunauer–Emmett–Teller (BET) analysis were conducted (**Figure 5**a,b).

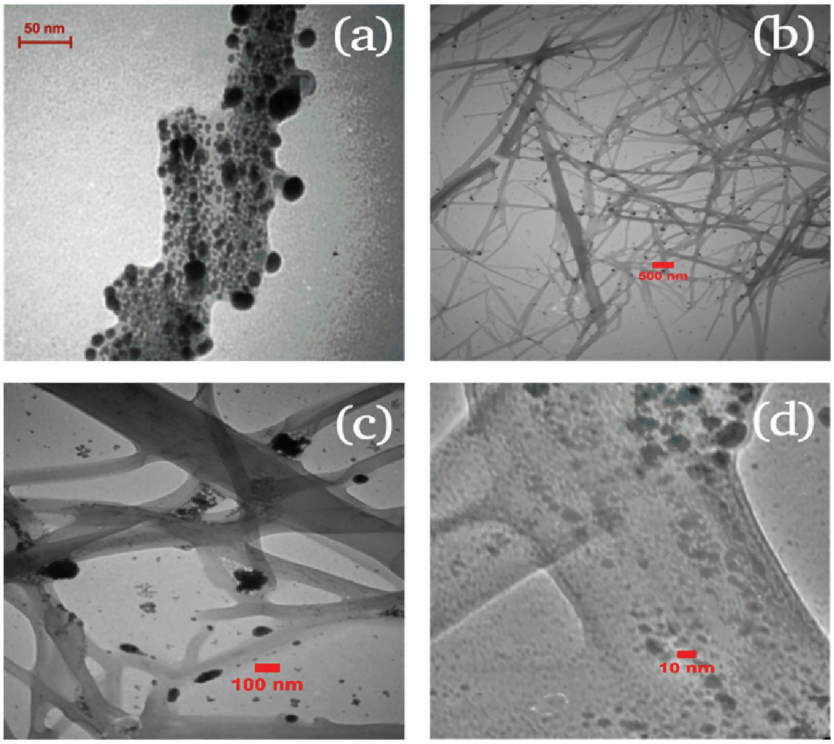

Figure 3. TEM images of a) Ag-MOF, and b–d) N1.

Table 2. Average sizes of N1, GO, and the MOF determined with the DLS analysis.

Specimen	A [nm]	B [nm]	C [nm]
N1	159	161	160
Ag-MOF	33.43	33.6	33.6
GO	79.2	79.2	78.8

A = average size by number. B = average size by volume. C = average size by intensity.

The adsorption/desorption results and the BET analysis data were summarized in **Table 3**. The mesoporous volume of N1 is 0.957 cm^3 g^{-1}, which is 3.5 times greater than that of the MOF. Total pore volume of the Ag-MOF increased from 0.0 017 652 into 0.0 053 038 cm^3 g^{-1} when combined with GO (N1 nanocomposite). Surface areas of GO, N1, N2, N3, and the Ag-MOF are 32.145, 4.168, 2.1553, 1.3057, and 1.2648 m^2 g^{-1}, respectively. As Figure 5a,b shows, there is a remarkable difference in the adsorption/desorption properties of GO and the other nanoparticles. Moreover, there is no considerable change in the adsorption/desorption properties of the Ag-MOF, N2, and N3 samples. The observed adsorption/desorption property of N1 is a result of the higher GO content of N1 compared to the Ag-MOF, N2, and N3. It is obvious that only GO and N1 nanocomposites have hysteresis in their adsorption/desorption diagram (Type3[61]), which is because of their higher mesoporous volume percent (Figure 5a,b).[62] The existence of mesoporous region in the nanocomposite affects the surface area value,[63] which is an important factor in antibacterial issues. The porosity of the samples increased with their GO content. As it can be seen, BET surface area of the nanocomposite increased with its GO content. The surface area is an important factor for biocidal activity.[64] These results imply that N1 is more active than the Ag-MOF, most likely because of its greater surface area.

2.2. Antibacterial Activity

We used optical density (OD) measurements (i.e., OD determined at a wavelength of 600 nm, OD_{600})[65–68] to evaluate changes in bacteria growth kinetics induced by N1 (and Ag-MOF) nanocomposites.[69–73] **Figure 6** shows the antibacterial activity of N1 against both *E. coli,* and *B. subtilis*. *E. coli* and *B. subtilis* bacteria in the early exponential phase with $OD_{600} \approx 0.15$ were exposed to 25 and 50 μg mL^{-1} N1 solutions, and the growth kinetics were monitored for 3 h. As shown, a 3 h exposure of the bacteria samples to 25 μg mL^{-1} N1 induces the growth of both bacteria strains in where the optical density of the treated bacteria to untreated bacteria (i.e., $OD_{600}^{Treat.}/OD_{600}^{Untreat.}$) decreases to ≈0.5 for *E. coli* and ≈0.4 for *B. subtilis*.

As depicted in Figure 6, the inducements in the growth kinetics of the bacteria strains

© 2018 WILEY-VCH Verlag GmbH & Co. KGaA, Weinheim

21967350, 2018, 11, Downloaded from https://onlinelibrary.wiley.com/doi/10.1002/admi.201701365 by Mostafa Dadashi Firouzjaei - University Of Alabama-Tuscaloosa , Wiley Online Library on [15/11/2024]. See the Terms and Conditions (https://onlinelibrary.wiley.com/terms-and-conditions) on Wiley Online Library for rules of use; OA articles are governed by the applicable Creative Commons License

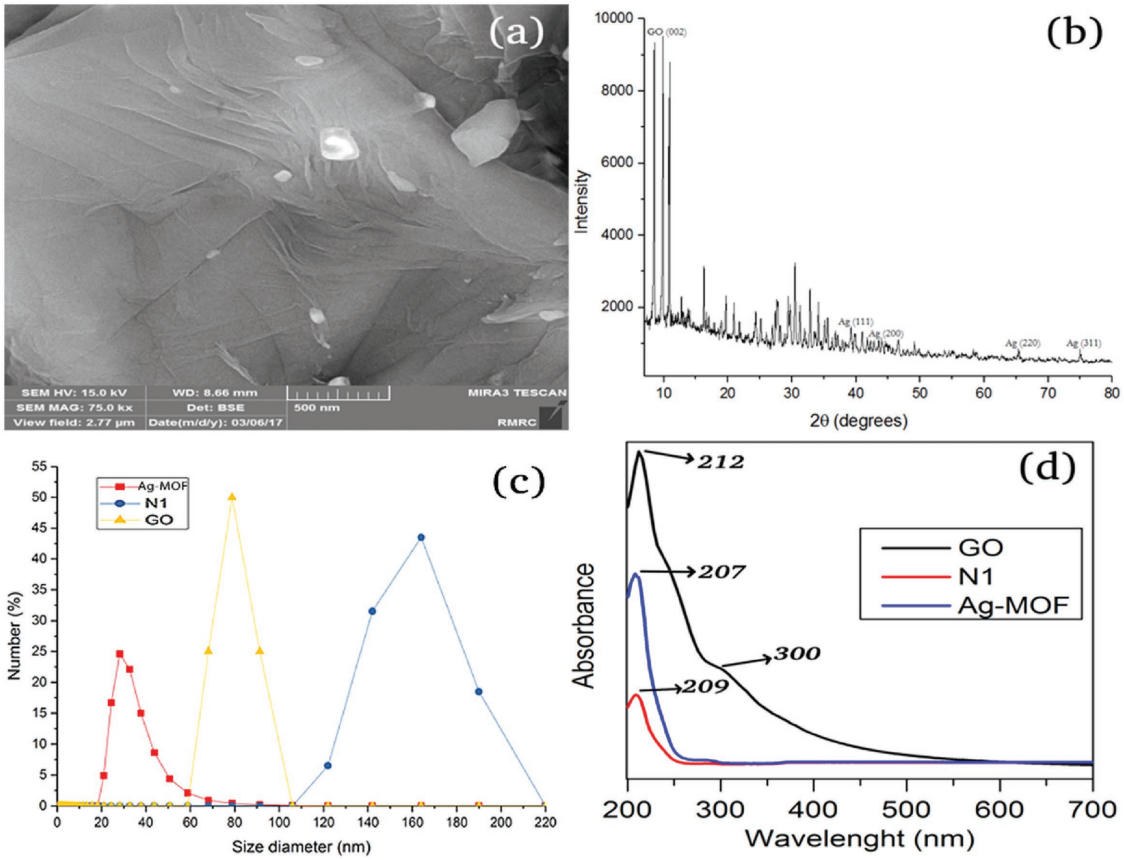

Figure 4. a) SEM image of N1, b) XRD pattern of N1, c) size distribution of N1, Ag-MOF, and GO, and d) UV–vis absorption spectra of Ag-MOF, N1, and GO.

are concentration-dependent; the higher concentration of 50 µg mL^{-1} N1 can immediately prevents growth of both bacteria species. To compare the antibacterial activity of N1 with the Ag-MOF, both strains were treated with 50 µg mL^{-1} of the nanoparticles. As depicted, N1 shows equal to higher antibacterial activity against both bacteria species. There results confirm that N1 has antibacterial activity against both *E. coli* and *B. subtilis* with the minimum inhibitory concentration of ≈50 µg mL^{-1} of the nanoparticles.

2.2.1. Flow Cytometric and Fluorescence Imaging of Ag-MOF and GO-Ag-MOF Treated Bacteria; E. coli versus B. subtilis

The importance of viability measurements of individual microorganisms has encouraged microbiologists, over decades, to introduce a variety of indicators to examine bacterial viability. Among the fluorescent probes, propidium iodide, PI, is a notable stain capable of assessing the viability of bacteria.[74,75] PI is known to exhibit a fluorescence enhancement (20- to 30-fold)

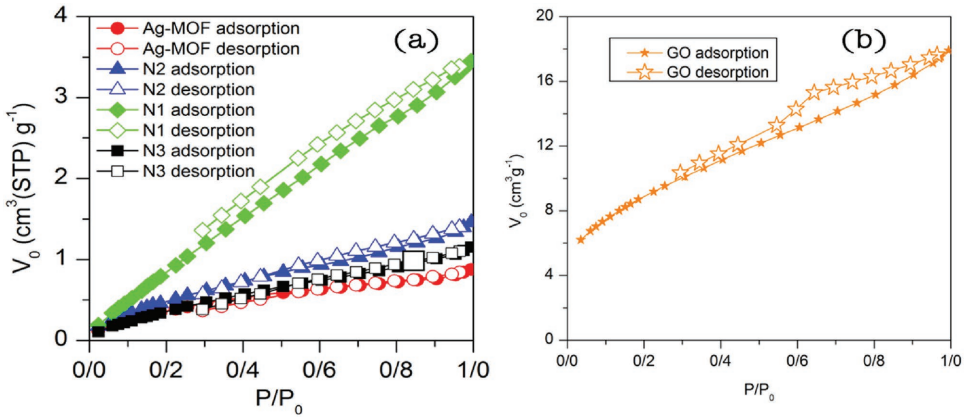

Figure 5. a) Nitrogen adsorption/desorption analysis of N1, N2, N3, and Ag-MOF, and b) nitrogen adsorption/desorption analysis of GO.

© 2018 WILEY-VCH Verlag GmbH & Co. KGaA, Weinheim

21967350, 2018, 11, Downloaded from https://onlinelibrary.wiley.com/doi/10.1002/admi.201701365 by Mostafa Dadashi Firouzjaei - University Of Alabama-Tuscaloosa , Wiley Online Library on [15/11/2024]. See the Terms and Conditions (https://onlinelibrary.wiley.com/terms-and-conditions) on Wiley Online Library for rules of use; OA articles are governed by the applicable Creative Commons License

Table 3. BET-plot analysis results.

Specimen	V_m [cm^3 g^{-1}]	a_s, BET [m^2 g^{-1}]	A [cm^3 g^{-1}]	B [nm]
GO	7.38	32.145	0.0275	3.433
N1	0.957	4.168	0.0053	5.09
N2	0.495	2.155	0.0022	4.148
N3	0.30	1.3057	0.0013	4.112
Ag-MOF	0.2906	1.2648	0.0017	5.582

A = total pore volume, B = mean pore diameter.

upon intercalation into double-stranded regions of DNA.[76,77] Given that bacterial DNA is found exclusively within the cytosol, such an interaction is feasible only if PI can diffuse across the cytoplasmic membrane (CM) of bacteria. Of significance, PI, with low concentration of $\leq 20 \times 10^{-6}$ M, does not cross the CM in live cells, which results in no fluorescence enhancement. However, dead bacteria exhibit a breakdown-induced CM permeability enhancement, which results in uptaking PI into the cytosol and then in fluorescence enhancement. Indeed, the integrity of the membrane of a cell plays an essential role in the cell viability. Therefore, fluorescence imaging (FI) and/or flow cytometry (FC) of bacteria incubated with low concentrations of PI is a convenient means of evaluating bacterial viability[78–82] and deducing mortality rates of cells exposed to a stimulus.[83,84] In contrast to PI, SYTO9 molecule can easily transport across the cytoplasmic membrane of both live and dead bacteria, which help estimate the ratio of dead/live bacteria (i.e., green for live and red for dead).

In this work, we used the complementary techniques, FI and FC, to evaluate antibacterial activity and mechanism-of-action of N1 against *E. coli* and *B. subtilis*. **Figure 7** depicts the FC and FI analyses of *E. coli* and *B. subtilis* treated with 100 μg mL^{-1} of N1 nanocomposite for ≈3 h. Figure 7a (left plot) depicts the contour plot of the forward angle scattering-area (FSC-A) versus the forward angle scattering-height (FSC-H) for the untreated *E. coli* sample. Because a bacteria cell is typically 1–2 μm, there is always a probability of having more than a single bacterium passing across the laser beam source in each event. Therefore, we use the FSC-A versus FSC-H contour plot to remove doublets (i.e., more than one bacteria in each event) from singlets (i.e., single bacteria in each event) in our FC analysis. This plot also shows the population of debris (i.e., including free biomolecules) at low FSC-A. Figure 7a (right plot) depicts the PI fluorescence signal of only the singlet population. This histogram depicts two regions: (1) The low-fluorescence cell population, which corresponds to the bacteria autofluorescence along with the fluorescence signal of free PI molecules; and (2) The high-fluorescence cell population, which corresponds to the florescence signal from PI molecules intercalated to the bacteria cytoplasmic DNA. Indeed, the dead bacteria population can be inferred from the second region of this histogram. Figure 7b provides the ratio of singlets-to-debris and the percent of dead bacteria within the singlets population for untreated and treated *E. coli* and *B. subtilis*. Given that all FC experiments were conducted using the same limit of 100 000 events, the singlets-to-debris ratio shows whether the bacteria were seriously damaged by the nanoparticle and the cytoplasmic contents were released from the bacteria. The percent of the dead bacteria, on the other hand, shows the increase in the population of the dead bacteria treated with the nanoparticles. Figure 7c,e presents the distributions of the PI fluorescence signals, obtained from the singlets, for *E. coli* and *B. subtilis*, which were treated with the nanoparticles. In fact, for samples with a higher percent of dead bacteria, the PI-fluorescence-signal distributions move to the right, indicating higher populations of PI-stained bacteria. The corresponding fluorescence images of the bacteria samples are presented in Figure 7d,f along with the percent of the dead bacteria (i.e., red/green). Figure 7 shows that N1 nanocomposite has strong antibacterial activity against both *E. coli* and *B. subtilis*. Indeed, the FC results confirms that 100 μg mL^{-1} of N1 nanocomposite increases the population of dead *E. coli* from ≈5 to 75% (i.e., compared with the 63% death rate for the bacteria treated with 100 μg mL^{-1} of Ag-MOF). The FI data give similar results; the percentage of the dead bacteria increased from ≈2% for untreated *E. coli* to 95 and 85% for *E. coli* treated with 100 μg mL^{-1} of N1 and the Ag-MOF, respectively. The singlets-to-debris ratio and FI results of *E. coli* confirm that the nanoparticles damage the bacteria, but the overall shape of the bacteria is not changed. However, *B. subtilis* shows a different behavior. In fact, both nanoparticles seriously damage *B. subtilis* in a way that the singlets-to-debris ratio of the bacteria significantly decreases (i.e., from ≈80 to 17% for both nanoparticles treatments). This effect is also observed from the FI results, indicating that a major fraction of *B. subtilis* population disappeared when treated with the nanoparticles (Figure 7f). However, the percentage of the dead *B. subtilis* within the singlets population increased from ≈4 to ≈78% for the untreated bacteria and to ≈70% for the bacteria treated with N1 and Ag-MOF nanoparticles.

The growth kinetics, FC, and FI results obtained for *E. coli* treated with N1 confirm that N1 has bactericidal activity against the bacteria strain. Specifically, the inducement in the growth kinetics indicates that the bacteria is affected by N1 and this effect is concentration-dependent. The FC and FI results

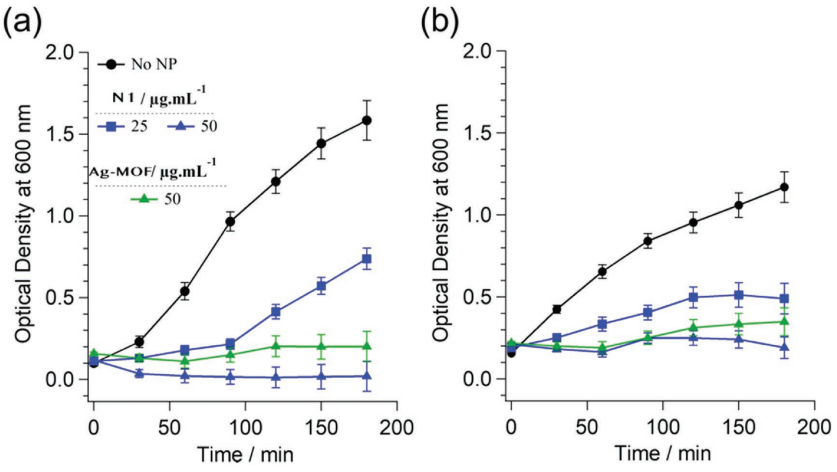

Figure 6. Growth kinetics of a) *E. coli* and b) *B. subtilis* at various concentrations of N1 (Ag-MOF is shown for comparison). The error bars were obtained from three separate experiments.

© 2018 WILEY-VCH Verlag GmbH & Co. KGaA, Weinheim

21967350, 2018, 11, Downloaded from https://onlinelibrary.wiley.com/doi/10.1002/admi.201701365 by Mostafa Dadashi Firouzjaei - University Of Alabama-Tuscaloosa , Wiley Online Library on [15/11/2024]. See the Terms and Conditions (https://onlinelibrary.wiley.com/terms-and-conditions) on Wiley Online Library for rules of use; OA articles are governed by the applicable Creative Commons License

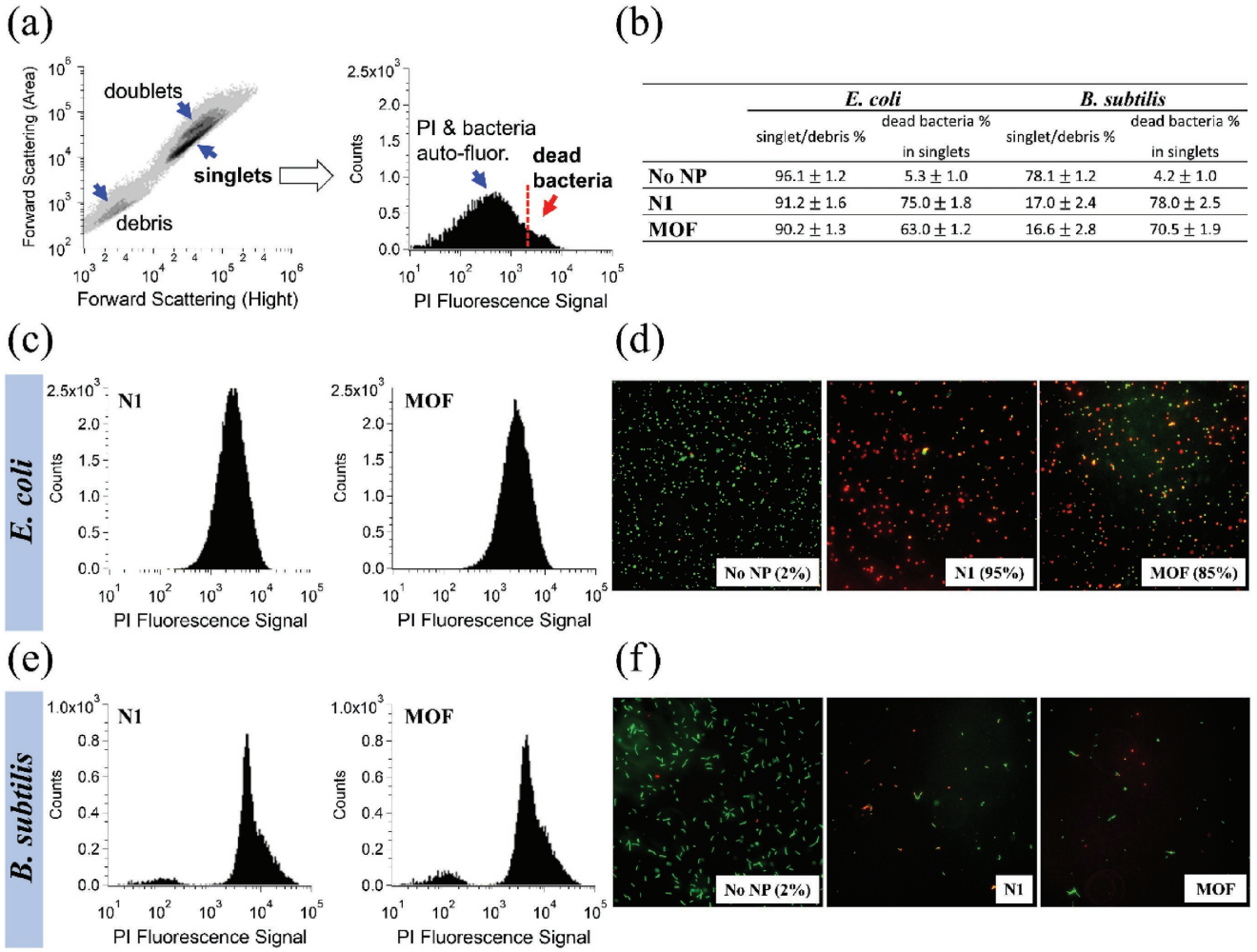

	E. coli		*B. subtilis*	
	singlet/debris %	dead bacteria % in singlets	singlet/debris %	dead bacteria % in singlets
No NP	96.1 ± 1.2	5.3 ± 1.0	78.1 ± 1.2	4.2 ± 1.0
N1	91.2 ± 1.6	75.0 ± 1.8	17.0 ± 2.4	78.0 ± 2.5
MOF	90.2 ± 1.3	63.0 ± 1.2	16.6 ± 2.8	70.5 ± 1.9

Figure 7. Antibacterial activity of N1 nanocomposite (compared with Ag-MOF) against *E. coli* and *B. subtilis*. a) Contour plot and PI fluorescence histogram of an untreated *E. coli* sample shown as an example of how to extract the information shown in (b), (c), and (e). Flow cytometry and fluorescence images of untreated bacteria and bacteria treated with 100 μg mL^{-1} of N1 and the MOF for ≈3 h, are shown in (c, e) and (d, f), respectively. The insets in the fluorescence images are the percent of the dead bacteria.

evidently suggest that N1 killed the majority of *E. coli* cells, however, the total number of the bacteria cells remained constant for both untreated and treated bacteria. Furthermore, N1 and the Ag-MOF showed "bacteriolytic" activity against *B. subtilis*. The FC and FI results indicate that N1 killed most of *B. subtilis* bacteria (i.e., both the total and viable cell counts decreased after treatment with N1).

The results showed that N1 has strong antibacterial activity against the Gram-positive and Gram-negative bacteria. The mechanism-of-action (MoA) of the nanocomposite may be different for the two bacteria species. More studies are needed to make conclusive statements on the antibacterial MoA of the nanocomposite. We plan to carry out such a study. Our current hypothesis for why the GO-Ag-MOF shows a higher antibacterial activity than Ag-MOF and GO alone is as follows. The isoelectric points of Gram-positive and Gram-negative bacteria cells have been reported to be in the ranges of 1.75–4.15 and 2.07–3.65, respectively.[85–87] As we conducted our experiments at a pH of 7.3, both bacterial species, which have negatively charged surfaces, are repelled by the negatively charged nanomaterials. Our measured zeta potentials of the Ag-MOF, GO, and N1 nanomaterials (–89.24, –57.74, and –51.66 mV, respectively) indicate that the N1 nanocomposite, which has the lowest electrostatic charge, should be repelled least by the bacteria, resulting in the highest probability of the interaction between the bacteria and N1, and thus the highest antibacterial activity.

3. Conclusions

A novel silver-based nanocomposite was developed by embellishing a silver-containing metal organic framework (Ag-MOF) with the GO. Characterization studies showed that the Ag-MOF nanoparticles were uniformly decorated on the GO nanosheet surfaces without any agglomeration. The results obtained using the growth curve, fluorescence imaging, and flow cytometry techniques showed the outstanding antibacterial activity of GO-Ag-MOF against *E. coli* and *B. subtilis*, and the higher toxicity of GO-Ag-MOF than those of the Ag-MOF and GO nanoparticles. Of significance is that GO-Ag-MOF and Ag-MOF

© 2018 WILEY-VCH Verlag GmbH & Co. KGaA, Weinheim

21967350, 2018, 11, Downloaded from https://onlinelibrary.wiley.com/doi/10.1002/admi.201701365 by Mostafa Dadashi Firouzjaei - University Of Alabama-Tuscaloosa , Wiley Online Library on [15/11/2024]. See the Terms and Conditions (https://onlinelibrary.wiley.com/terms-and-conditions) on Wiley Online Library for rules of use; OA articles are governed by the applicable Creative Commons License

extirpated 95 and 85% of the live bacteria cells, respectively. The results suggest that the GO-Ag-MOF is a promising strongly antimicrobial composite for biomedical applications.

4. Experimental Section

Materials: Silver nitrate ($AgNO_3$), BTC, and ethanol (purity, 99%) were purchased from Merck, Germany. Graphene-oxide (US7906) was received from US Research Nanomaterial, Inc. *E. coli* ATCC 35695 and *B. subtilis* ATCC 23857 were supplied by ATCC Company. Terrific Broth (TB) and propidium iodide (PI) were obtained from Sigma-Aldrich, and SYTO9 from Molecular Probes. Glycerin was received from Fisher Scientific.

Synthesis of Nanoparticles: For the synthesis of GO-MOF nanoparticles, ultrasonic irradiation was applied at a frequency of 20 KHz (Heilscher UP400s, Germany) for a reaction time of 60 min. During the ultrasonic irradiation, output energy, and pulse were kept at 100 W and 0.6, respectively. First, two homogenous solutions – 0.5 g of BTC dissolved in 20 mL of ethanol and 0.5 g of silver nitrate dissolved in 20 mL of deionized water – were prepared. The two solutions were then added to three GO suspensions [50, 35, and 25 mg of GO in 10 mL of deionized-water], and the resulting mixtures were sonicated for 60 min in room temperature (**Scheme 1**). After the ultrasonic step, the mixtures were left for 12 h to obtain brown precipitates. The precipitates were dried in a 35 °C oven for 24 h. The precipitates (Ag-MOF/GO nanocomposites) prepared with the 50, 35, and 25 mg of GO were labeled as N1, N2, and N3, respectively.

Characterization: To identify the functional groups of the nanoparticles, attenuated total reflection-Fourier transform infrared (ATR-FTIR) spectroscopy was conducted using a Spectrum One ATR-FTIR spectrometer (Varian Excalibur FTS-3000) with 16 scans and a resolution of 4 cm^{-1}. XRD patterns were recorded at 298 K using an XPERT-PRO X-ray diffractometer to determine the nanoparticles crystalline structure. An XPS (Bestec, Germany) equipped with a 100 µm monochromatic Al Kα X-ray photoelectron spectrometer source was employed to determine the elemental composition of the nanoparticles. A hemispherical electron energy analyzer was utilized to collect the emitted photoelectrons.

The morphology of the synthesized nanomaterials was examined using a TEM (Zeiss EM900), operated at 20 KV. For sample preparation, the nanomaterials were stabilized in water via sonication, then a drop of the stabilized solution was placed onto a TEM grid and dried in a vacuum oven at ambient temperature. TEM images of the GO sample were provided by the manufacturer. The surface morphology of the specimens was observed via Vega SEM (TESCAN-LMU). For sample preparation, nanoparticles were placed on a carbon tape and were then coated with a thin layer of gold using a sputter coater.

The size of the nanoparticles was measured via dynamic light scattering (DLS, Nano ZS ZEN 3600). First, the samples were stabilized in water (0.5 M concentration of the samples) using sonication. The size distribution of the specimens was determined with volume, intensity, and number of peaks. The zeta potential of the nanoparticles was measured using Brookhaven Instruments. The final value for each sample was the average of 3 runs with 30 cycles per run. Absorption spectra for the nanoparticles were obtained using a UV–Vis spectrophotometer (PerkinElmer LAMBDA 35). To determine the pore size distribution and surface area of the nanoparticles, N_2 adsorption–desorption was performed at 77 K using a Belsorp mini 2. The BET and the Barrett–Joyner–Halenda methods were used to calculate the specific surface area of each specimen. At first, all samples were degassed under vacuum for 24 h to eliminate any impurity and water.

Antibacterial Investigations – Bacteria Strains: The antibacterial properties of N1 and Ag-MOF nanoparticles were evaluated using Gram-negative *E. coli* (mc4100 strain, ATCC 35695) and Gram-positive *B. subtilis* strains (Ehrenberg Cohn 168 strain, ATCC 23857). The bacteria strains were cultivated on Lauria Broth agar medium plates (LB Broth with agar Lennox, Cat. No.: L2897, Sigma-Aldrich) at 37 °C for ≈24 h and then stored at 4 °C for future use.

Antibacterial Investigations – Bacteria Growth Kinetic: A discrete colony of each bacteria strain was grown aerobically at 37 °C in 50 mL TB culture media in a flask shaking at 150 rpm. The TB media was made of 9.52 g Terrific Broth (Cat. No.: T0918, Sigma-Aldrich) and 1.6 mL glycerin (Cat. No.: G31-1, Fisher Scientific, USA) in 200 mL distilled deionized water (Millipore, 18.2 MΩ cm) and was autoclaved at 121 °C for 20 min. Bacteria growth kinetics were measured by

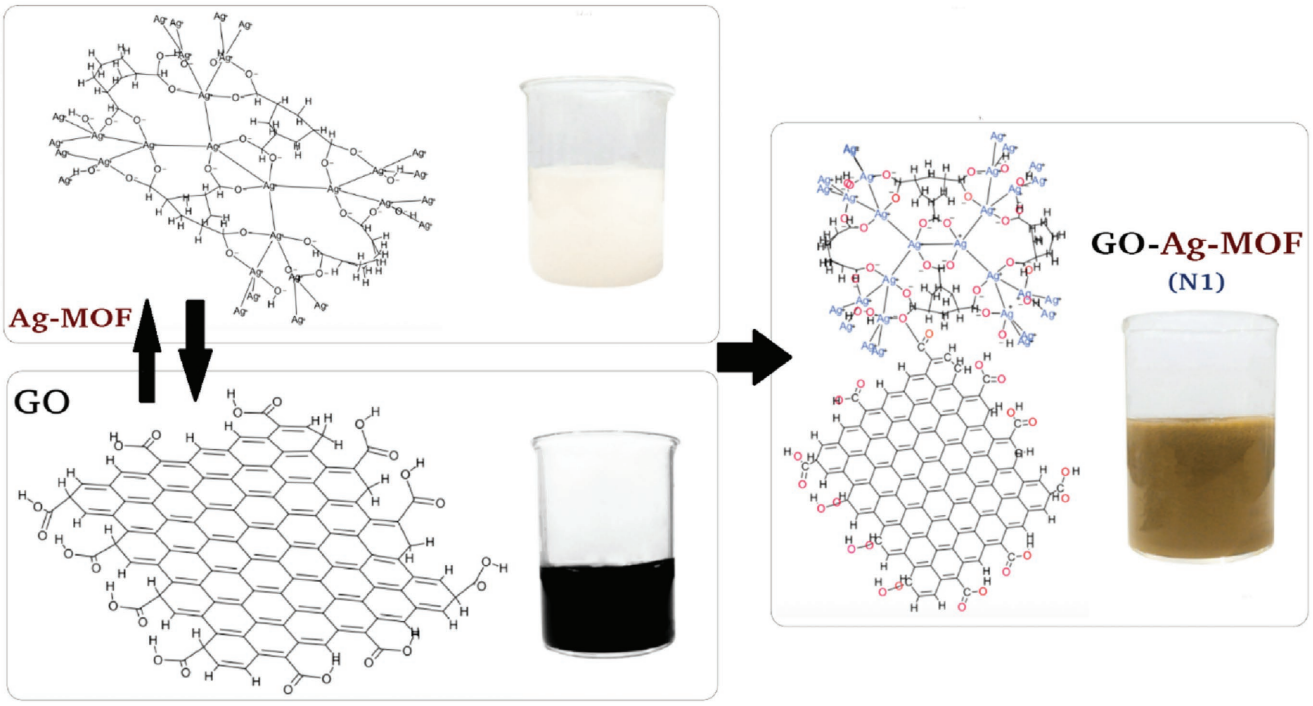

Scheme 1. Preparation steps of the GO-Ag-MOF nanocomposites.

© 2018 WILEY-VCH Verlag GmbH & Co. KGaA, Weinheim

21967350, 2018, 11, Downloaded from https://onlinelibrary.wiley.com/doi/10.1002/admi.201701365 by Mostafa Dadashi Firouzjaei - University Of Alabama-Tuscaloosa , Wiley Online Library on [15/11/2024]. See the Terms and Conditions (https://onlinelibrary.wiley.com/terms-and-conditions) on Wiley Online Library for rules of use; OA articles are governed by the applicable Creative Commons License

monitoring the optical density of the bacteria suspensions at 600 nm (i.e., OD_{600}).

After about 4 h of growth (i.e., at early exponential phase with $OD_{600} = 0.15 \pm 0.05$), 1 mL of the harvested bacteria strains were transferred into 1 mL cuvettes to prepare untreated and treated bacteria samples with various concentrations of the nanoparticles and allow bacteria samples grow in the cuvettes on the shaker at 37 °C and 150 rpm (i.e., nanoparticle stock suspensions of 200 μg mL^{-1} were sonicated at 37 kHz for ≈4 h before use). The OD_{600} values of the suspensions were recorded every 30 min for 3 h.

Antibacterial Investigations – Bacteria Preparation for Imaging and Cytometry Assays: A discrete colony of each bacteria strain was grown aerobically at 37 °C in a 50 mL TB culture media in a flask shaking at 150 rpm for ≈8 h (i.e., at middle-to-late exponential phase). The harvested bacteria were centrifuged (i.e., 1500xg, 2 min, room temperature) and then washed twice with enough amount of phosphate buffered saline (i.e., 1xPBS; pH = 7.3) to remove waste and residual TB. For each washing step, a Rotamix (10101-RKVSD, ATR Inc.) was used at 20 rpm to suspend the pellet cells in 1xPBS with no biomechanical forces applied to bacteria during the resuspensions. After twice washing with enough 1xPBS, the supernatant was removed and the pellets were collected for preparing the *E. coli* and *B. subtilis* stock samples in 1xPBS with the cell density of $OD_{600} = 0.15 \pm 0.05$.

Antibacterial Investigations – Fluorescence Imaging of Bacteria: In each fluorescence imaging experiment, 20 μL aliquot of the untreated and treated bacteria suspensions were added onto microscope glass slides to perform the viability staining. For treated samples, bacteria stock samples were exposed to 100 μg mL^{-1} of each nanoparticle for ≈3 h (i.e., nanoparticle stock suspensions of 200 μg mL^{-1} were sonicated at 37 kHz for ≈4 h before use). The samples were then incubated with 20×10^{-6} M propidium iodide, PI (Sigma-Aldrich) and 5×10^{-6} M SYTO9 (Molecular Probes) for ≈15 min in dark at room temperature. To avoid any osmotic stress on bacteria samples, the PI/SYTO9 solution was prepared in 1xPBS. The samples were enclosed by glass coverslip slides and were mounted on the microscope stage. Epi-fluorescence images of at least 15 field-of-view (FOV) were recorded for each glass slide (i.e., each sample) and more than 2000 cells were counted for three separate experiments. The SYTO9-stained bacteria (i.e., green) correspond to the live cells and the PI-stained bacteria (i.e., red) correspond to the dead cells. The percent of live cells was calculated using the two values.

Antibacterial Investigations – Fluorescence Microscope Setup and Image Analysis: A Nikon ECLIPSE TE200 microscope with a 40x/0.60 Plan Flour (Nikon) objective len and a digital image capture system (Hamamatsu C11440) was used, and images were recorded by the NIS Elements (ver. 4.20) software. For the fluorescence imaging, epi-fluorescence scheme was used. A EXFO X-cite 120 Fluorescence Illuminator system was used as the light source to excite the PI and SYTO9 molecules, and the red and green fluorescence emissions were recorded in backward direction through appropriate filter cubes. The filter cubes had an excitation and detection wavelengths centered at 560 and 630 nm for PI (Prod. No.: 49008, CHROMA) and 480 and 535 nm for SYTO9 molecules (Prod. No.: 49011, CHROMA). Image analysis was performed in ImageJ (National Institutes of Health, 1.43u). In a typical image analysis, the images recorded by the two filter cubes were stacked to show the PI-stained and SYTO9-stained bacteria in a single FOV.

Antibacterial Investigations – Flow Cytometry of Bacteria: Bacteria stock samples were exposed to 100 μg mL^{-1} of each nanoparticle for ≈3 h (i.e., nanoparticle stock suspensions of 200 μg mL^{-1} were sonicated at 37 kHz for ≈4 h before use). 100 μL of each treated and untreated samples were added into a 96 flat-bottom well microtiter plate and incubated with 20×10^{-6} M propidium iodide and 5×10^{-6} M SYTO9 in 1xPBS (i.e., 1xPBS was used to avoid osmotic shock) for ≈15 min in dark at room temperature. Samples were then placed onto the flow cytometer (BD Accuri® C6 Flow Cytometer) for analysis. The FC analysis ran with a medium fluid rate and limits of 100 000 events. The PI and SYTO9 were illuminated with a 15 mW argon ion laser (488 nm), and their fluorescence signals were collected through the FL2 and FL1 channels with the detection wavelengths of 585 ± 20 and 533 ± 15 nm, respectively. Three FC trials were attempted on each sample for three separate bacteria suspensions to obtain statistically acceptable results. The fluorescence signals and the FSC signal were amplified with the logarithmic mode. The FC data were analyzed by the BD Accuri C6 software.

No considerable change was observed for the antibacterial activity of the Ag-MOF and those of N2 and N3 nanoparticles, most likely due to the low concentration of GO in the N2 and N3 structures. Therefore, among the GO-Ag-MOFs, N1 that has the highest GO content, was studied extensively, and its antibacterial activity was compared to those of GO and Ag-MOF nanoparticles.

Acknowledgements

M.D.F. and A.A.S. contributed equally to this work.

Conflict of Interest

The authors declare no conflict of interest.

Keywords

antibacterial properties, graphene oxide, metal-organic framework, nanocomposites, nanomaterials, silver

Received: October 21, 2017
Revised: January 28, 2018
Published online: April 3, 2018

[1] W. Shao, X. Liu, H. Min, G. Dong, Q. Feng, S. Zuo, *ACS Appl. Mater. Interfaces* **2015**, *7*, 6966.
[2] M.-C. Wu, A. R. Deokar, J.-H. Liao, P.-Y. Shih, Y.-C. Ling, *ACS Nano* **2013**, *7*, 1281.
[3] I. Sondi, B. Salopek-Sondi, *J. Colloid Interface Sci.* **2004**, *275*, 177.
[4] M. I. Katsnelson, *Mater. Today* **2007**, *10*, 20.
[5] F. Guo, G. Silverberg, S. Bowers, S.-P. Kim, D. Datta, V. Shenoy, R. H. Hurt, *Environ. Sci. Technol.* **2012**, *46*, 7717.
[6] Y. Shen, Q. Fang, B. Chen, *Environ. Sci. Technol.* **2015**, *49*, 67.
[7] V. Chabot, D. Higgins, A. Yu, X. Xiao, Z. Chen, J. Zhang, *Energy Environ. Sci.* **2014**, *7*, 1564.
[8] F. Kim, L. J. Cote, J. Huang, *Adv. Mater.* **2010**, *22*, 1954.
[9] D. R. Dreyer, S. Park, C. W. Bielawski, R. S. Ruoff, *Chem. Soc. Rev.* **2010**, *39*, 228.
[10] W. Gao, L. B. Alemany, L. Ci, P. M. Ajayan, *Nat. Chem.* **2009**, *1*, 403.
[11] S. S. Nanda, D. K. Yi, K. Kim, *Scientific Reports* **2016**, *6*, 28443.
[12] O. Akhavan, E. Ghaderi, A. Esfandiar, *J. Phys. Chem. B* **2011**, *115*, 6279.
[13] O. Akhavan, E. Ghaderi, *ACS Nano* **2010**, *4*, 5731.
[14] W. Hu, C. Peng, W. Luo, M. Lv, X. Li, D. Li, Q. Huang, C. Fan, *ACS Nano* **2010**, *4*, 4317.
[15] G. P. Kotchey, B. L. Allen, H. Vedala, N. Yanamala, A. A. Kapralov, Y. Y. Tyurina, J. Klein-Seetharaman, V. E. Kagan, A. Star, *ACS Nano* **2011**, *5*, 2098.
[16] F. Perreault, A. F. De Faria, S. Nejati, M. Elimelech, *ACS Nano* **2015**, *9*, 7226.
[17] W. Bing, Z. Chen, H. Sun, P. Shi, N. Gao, J. Ren, X. Qu, *Nano Res.* **2015**, *8*, 1648.
[18] S.-L. Loo, W. B. Krantz, X. Hu, A. G. Fane, T.-T. Lim, *J. Colloid Interface Sci.* **2016**, *461*, 104.
[19] F. Huang, Y. Gao, Y. Zhang, T. Cheng, H. Ou, L.-J. Yang, J. Liu, L. Shi, J. Liu, *ACS Appl. Mater. Interfaces* **2017**, *9*, 16880.

© 2018 WILEY-VCH Verlag GmbH & Co. KGaA, Weinheim

21967350, 2018, 11, Downloaded from https://onlinelibrary.wiley.com/doi/10.1002/admi.201701365 by Mostafa Dadashi Firouzjaei - University Of Alabama-Tuscaloosa , Wiley Online Library on [15/11/2024]. See the Terms and Conditions (https://onlinelibrary.wiley.com/terms-and-conditions) on Wiley Online Library for rules of use; OA articles are governed by the applicable Creative Commons License

[20] F. Cao, E. Ju, Y. Zhang, Z. Wang, C. Liu, W. Li, Y. Huang, K. Dong, J. Ren, X. Qu, *ACS Nano* **2017**, *11*, 4651.
[21] R. Zhao, M. Lv, Y. Li, M. Sun, W. Kong, L. Wang, S. Song, C. Fan, L. Jia, S. Qiu, *ACS Appl. Mater. Interfaces* **2017**, *9*, 15328.
[22] X. Ran, Y. Du, Z. Wang, H. Wang, F. Pu, J. Ren, X. Qu, *ACS Appl. Mater. Interfaces* **2017**, *9*, 19717.
[23] S. R. Batten, N. R. Champness, X.-M. Chen, J. Garcia-Martinez, S. Kitagawa, L. Öhrström, M. O'Keeffe, M. Paik Suh, J. Reedijk, *Pure Appl. Chem.* **2013**, *85*, 1715.
[24] W. Lin, *J. Solid State Chem.* **2005**, *178*, 2486.
[25] H.-C. "Joe" Zhou, S. Kitagawa, *Chem. Soc. Rev.* **2014**, *43*, 5415.
[26] T.-H. Chen, I. Popov, W. Kaveevivitchai, O. Š. Miljanić, *Chem. Mater.* **2014**, *26*, 4322.
[27] C. Orellana-Tavra, E. F. Baxter, T. Tian, T. D. Bennett, N. K. H. Slater, A. K. Cheetham, D. Fairen-Jimenez, *Chem. Commun.* **2015**, *51*, 13878.
[28] M. Usman, S. Mendiratta, K.-L. Lu, *Adv. Mater.* **2017**, *29*, 1605071.
[29] A. M. Fracaroli, H. Furukawa, M. Suzuki, M. Dodd, S. Okajima, F. Gándara, J. A. Reimer, O. M. Yaghi, *J. Am. Chem. Soc.* **2014**, *136*, 8863.
[30] T. Rodenas, I. Luz, G. Prieto, B. Seoane, H. Miro, A. Corma, F. Kapteijn, F. X. Llabrés i Xamena, J. Gascon, *Nat. Mater.* **2014**, *14*, 48.
[31] H.-C. Zhou, J. R. Long, O. M. Yaghi, *Chem. Rev.* **2012**, *112*, 673.
[32] A. U. Czaja, N. Trukhan, U. Müller, *Chem. Soc. Rev.* **2009**, *38*, 1284.
[33] X.-L. Zhao, W.-Y. Sun, *CrystEngComm* **2014**, *16*, 3247.
[34] C. V. McGuire, R. S. Forgan, *Chem. Commun.* **2015**, *51*, 5199.
[35] N. V. Fischer, A. Inayat, W. Schwieger, N. Burzlaff, *J. Coord. Chem.* **2010**, *63*, 2831.
[36] D.-M. Chen, N. Xu, X.-H. Qiu, P. Cheng, *Cryst. Growth Des.* **2015**, *15*, 961.
[37] H. Furukawa, K. E. Cordova, M. O'Keeffe, O. M. Yaghi, *Science* **2013**, *341*, 1230444.
[38] H. Kobayashi, Y. Mitsuka, H. Kitagawa, *Inorg. Chem.* **2016**, *55*, 7301.
[39] M. Dincă, J. R. Long, *Angew. Chem., Int. Ed.* **2008**, *47*, 6766.
[40] Z. Wang, S. M. Cohen, *Chem. Soc. Rev.* **2009**, *38*, 1315.
[41] S. Das, H. Kim, K. Kim, *J. Am. Chem. Soc.* **2009**, *131*, 3814.
[42] A. Pichon, S. L. James, *CrystEngComm* **2008**, *10*, 1839.
[43] D. Braga, S. L. Giaffreda, F. Grepioni, M. R. Chierotti, R. Gobetto, G. Palladino, M. Polito, *CrystEngComm* **2007**, *9*, 879.
[44] I. Stassen, M. Styles, G. Grenci, H. Van Gorp, W. Vanderlinden, S. De Feyter, P. Falcaro, D. De Vos, P. Vereecken, R. Ameloot, *Nat. Mater.* **2015**, *15*, 304.
[45] Z. Ni, R. I. Masel, *J. Am. Chem. Soc.* **2006**, *128*, 12394.
[46] W. Zhuang, D. Yuan, J.-R. Li, Z. Luo, H.-C. Zhou, S. Bashir, J. Liu, *Adv. Healthcare Mater.* **2012**, *1*, 225.
[47] M. Cavicchioli, A. C. Massabni, T. A. Heinrich, C. M. Costa-Neto, E. P. Abrão, B. A. L. Fonseca, E. E. Castellano, P. P. Corbi, W. R. Lustri, C. Q. F. Leite, *J. Inorg. Biochem.* **2010**, *104*, 533.
[48] P. Horcajada, T. Chalati, C. Serre, B. Gillet, C. Sebrie, T. Baati, J. F. Eubank, D. Heurtaux, P. Clayette, C. Kreuz, J.-S. Chang, Y. K. Hwang, V. Marsaud, P.-N. Bories, L. Cynober, S. Gil, G. Ferey, P. Couvreur, R. Geref, *Nat. Mater.* **2010**, *9*, 172.
[49] G. Wyszogrodzka, B. Marszałek, B. Gil, P. Dorożyński, *Drug Discovery Today* **2016**, *21*, 1009.
[50] X. Lu, J. Ye, D. Zhang, R. Xie, R. F. Bogale, Y. Sun, L. Zhao, Q. Zhao, G. Ning, *J. Inorg. Biochem.* **2014**, *138*, 114.
[51] X. Zhou, Y. Zhang, Z. Huang, D. Lu, A. Zhu, G. Shi, *Sci. Rep.* **2016**, *6*, srep38417.
[52] C. Tao, J. Wang, S. Qin, Y. Lv, Y. Long, H. Zhu, Z. Jiang, *J. Mater. Chem.* **2012**, *22*, 24856.
[53] S. Frindy, A. Primo, H. Ennajih, A. el Kacem Qaiss, R. Bouhfid, M. Lahcini, E. M. Essassi, H. Garcia, A. El Kadib, *Carbohydr. Polym.* **2017**, *167*, 297.
[54] S. Pei, H.-M. Cheng, *Carbon* **2012**, *50*, 3210.
[55] A. M. Ferraria, A. P. Carapeto, A. M. B. do Rego, *Vacuum* **2012**, *86*, 1988.
[56] B.-T. Qu, J.-C. Lai, S. Liu, F. Liu, Y.-D. Gao, X.-Z. You, *Cryst. Growth Des.* **2015**, *15*, 1707.
[57] C. Deetuam, C. Samthong, S. Thongyai, P. Praserthdam, A. Somwangthanaroj, *Compos. Sci. Technol.* **2014**, *93*, 1.
[58] J. Tang, Q. Chen, L. Xu, S. Zhang, L. Feng, L. Cheng, H. Xu, Z. Liu, R. Peng, *ACS Appl. Mater. Interfaces* **2013**, *5*, 3867.
[59] Y. Ouyang, X. Cai, Q. Shi, L. Liu, D. Wan, S. Tan, Y. Ouyang, *Colloids Surf., B* **2013**, *107*, 107.
[60] A. F. de Faria, A. C. M. de Moraes, P. D. Marcato, D. S. T. Martinez, N. Durán, A. G. Souza Filho, A. Brandelli, O. L. Alves, *J. Nanopart. Res.* **2014**, *16*, 2110.
[61] S. Lowell, J. E. Shields, M. A. Thomas, M. Thommes, *Characterization of Porous Solids and Powders: Surface Area, Pore Size and Density*, Springer Science & Business Media, Dordrecht, The Netherlands **2012**.
[62] M. Thommes, B. Smarsly, M. Groenewolt, P. I. Ravikovitch, A. V. Neimark, *Langmuir* **2006**, *22*, 756.
[63] A. Galarneau, Z. Abid, B. Said, Y. Didi, K. Szymanska, A. Jarzębski, F. Tancret, H. Hamaizi, A. Bengueddach, F. Di Renzo, *Inorganics* **2016**, *4*, 9.
[64] K. Kavitha, S. Sutha, M. Prabhu, V. Rajendran, T. Jayakumar, *Carbohydr. Polym.* **2013**, *93*, 731.
[65] M. Scott, C. W. Gunderson, E. M. Mateescu, Z. Zhang, T. Hwa, *Science* **2010**, *330*, 1099.
[66] S. Klumpp, Z. Zhang, T. Hwa, *Cell* **2009**, *139*, 1366.
[67] F. C. Neidhardt, *Escherichia Coli and Salmonella: Cellular and Molecular Biology*, ASM Press, Washington, DC **1996**.
[68] M. T. Madigan, J. M. Martinko, D. A. Stahl, D. P. Clark, *Brock Biology of Microorganisms*, Benjamin Cummings, Boston **2012**, 49.
[69] B. R. Levin, K. I. Udekwu, *Antimicrob. Agents Chemother.* **2010**, *54*, 3414.
[70] S. A. Holowachuk, M. F. Bal'a, R. K. Buddington, *J. Microbiol. Methods* **2003**, *55*, 441.
[71] T. Bollenbach, S. Quan, R. Chait, R. Kishony, *Cell* **2009**, *139*, 707.
[72] J. M. Andrews, *J. Antimicrob. Chemother.* **2001**, *48*, 5.
[73] K. Theophel, V. J. Schacht, M. Schlüter, S. Schnell, C. S. Stingu, R. Schaumann, M. Bunge, *Front. Microbiol.* **2014**, *5*, 544.
[74] L. I. Grossman, R. Watson, J. Vinograd, *J. Mol. Biol.* **1974**, *86*, 271.
[75] C. J. G. Yeh, B.-L. Hsi, W. P. Faulk, *J. Immunol. Methods* **1981**, *43*, 269.
[76] J. Tas, G. Westerneng, *J. Histochem. Cytochem.* **1981**, *29*, 929.
[77] B. Hudson, W. B. Upholt, J. Devinny, J. Vinograd, *Proc. Natl. Acad. Sci. USA* **1969**, *62*, 813.
[78] R. Löpez-Amorós, S. Castel, J. Comas-Riu, J. Vives-Rego, *Cytometry* **1997**, *29*, 298.
[79] R. Lopez-Amoros, J. Comas, J. Vives-Rego, *Appl. Environ. Microbiol.* **1995**, *61*, 2521.
[80] R. I. Jepras, J. Carter, S. C. Pearson, F. E. Paul, M. J. Wilkinson, *Appl. Environ. Microbiol.* **1995**, *61*, 2696.
[81] N. Banning, S. Toze, B. J. Mee, *J. Appl. Microbiol.* **2002**, *93*, 69.
[82] S. C. Williams, Y. Hong, D. C. Danavall, M. H. Howard-Jones, D. Gibson, M. E. Frischer, P. G. Verity, *J. Microbiol. Methods* **1998**, *32*, 225.
[83] M. P. Singh, *J. Microbiol. Methods* **2006**, *67*, 125.
[84] O. N. Mileyeva-Biebesheimer, A. Zaky, C. L. Gruden, *Environ. Eng. Sci.* **2010**, *27*, 329.
[85] T. J. Beveridge, *Int. Rev. Cytol.* **1981**, *72*, 229.
[86] V. P. Harden, J. O. Harris, *J. Bacteriol.* **1953**, *65*, 198.
[87] C. Scharf, R. Schmid, U. Mäder, C. Eymann, H. Antelmann, A. Völker, U. Völker, M. Hecker, *Electrophoresis* **2001**, *22*, 2908.

© 2018 WILEY-VCH Verlag GmbH & Co. KGaA, Weinheim

21967350, 2018, 11, Downloaded from https://onlinelibrary.wiley.com/doi/10.1002/admi.201701365 by Mostafa Dadashi Firouzjaei - University Of Alabama-Tuscaloosa , Wiley Online Library on [15/11/2024]. See the Terms and Conditions (https://onlinelibrary.wiley.com/terms-and-conditions) on Wiley Online Library for rules of use; OA articles are governed by the applicable Creative Commons License